Research Article

# In-situ fabrication of ZnO thin film electrode using spent Zn–C battery and its electrochemical performance for supercapacitance

Kamrul Hassan[1] · Rifat Farzana[1] · Veena Sahajwalla[1]



**Abstract**
In consideration of effective supercapacitors which are also affordable and lightweight, metal oxides can be considered because of the higher charge storage capability. This work establishes the in situ fabrication of a supercapacitor electrode, employing spent Zn–C batteries as precursor. Every year, extensive number of waste batteries including Zn–C battery end up in landfill, which prolonged the compulsion of waste disposal in landfill and creates environmental and health threat. The transformation of waste battery materials into fabricating components for energy applications, is of great significance for sustainable strategies but it is a challenging work to produce nanomaterials with purity by green methods. The present study proposes the in situ fabrication of ZnO NPs as ultra-thin film on a porous silicon (P-Si) substrate from spent Zn–C battery at 900 °C in the horizontal tube furnace under argon atmosphere. The particles were around 45 nm size and semi-spherical in morphology and showed uniform distributions all over the substrate as a discrete ultra-thin film. The ZnO ultra-thin film basically comprised of several ZnO film layer which stacked with each other periodically and made one thin layer of ~ 390 nm, where the single layer was ~ 45 nm. Formation of ZnO NPs were detected by the analysis of XRD, EDS and XPS. Using cyclic voltammetry as well as impedance spectroscopy in 0.6 M KOH as electrolyte, electrochemical properties of developed electrodes and supercapacitor have also been examined. The ZnO/P-Si electrode demonstrated a highest value of specific capacitance 547 F $g^{-1}$ at 5 mV $s^{-1}$ scan rate. Obtained results demonstrate that spent Zn–C battery can be selected to fabricate the energy storage devices which can offer economical, technological and environmental advantages.

**Keywords** Spent Zn–C battery · ZnO NPs · Ultra-thin film · Supercapacitor · Sustainability

## 1 Introduction

Supercapacitors are kind of electrochemical capacitors which are charge storage device that have got attention owing to higher specific energy than the conventional capacitors along with their greater density of power than the batteries [1, 2]. Generally, two types of electrode materials have been used to fabricate the supercapacitor: (1) carbon materials having higher surface area, for instance carbon aerogel and activated carbon etc. [3]; (2) metal oxides for example oxides of Ni, Ru, Co and Zn etc., and polymers with conduction properties [4]. Because of having the higher specific capacitance and noticeable electrochemical properties, ruthenium (Ru) oxides are broadly used in the electrochemical supercapacitor [5]. However, commercial acceptance of Ru has been abated because of the high cost and a cheap metal oxide such as transition metal oxides with numerous oxidation states has become popular for the supercapacitor application. Nickel oxide (NiO) [6–8], cobalt oxide (CoO) [9] and manganese

**Electronic supplementary material** The online version of this article (https://doi.org/10.1007/s42452-019-0302-1) contains supplementary material, which is available to authorized users.

✉ Rifat Farzana, r.farzana@unsw.edu.au | [1]Centre for Sustainable Materials Research and Technology (SMaRT@UNSW), School of Materials Science and Engineering, UNSW Sydney, Sydney, NSW 2052, Australia.

SN Applied Sciences (2019) 1:302 | https://doi.org/10.1007/s42452-019-0302-1

Received: 10 December 2018 / Accepted: 25 February 2019 / Published online: 5 March 2019

oxide (MnO) supercapacitors [10], are low-priced and have pseudocapacitive behavior like the ruthenium oxide. The various physical properties of nanoparticles of zinc oxide (ZnO) are widely accessible [11–14] in literature but the pertinence of ZnO as an important candidate for application of supercapacitor is less reported. ZnO nanoparticles are in chief striking for forthcoming applications because of biocompatible, environmentally friendly, possession of high electron mobility and relatively inexpensive properties of them. Most importantly, because of the high energy density, ZnO is renowned as battery active material though it can have disadvantage to form of dendrite development during the successive cycling, which can decrease in cycle life. Still, owing to its ecofriendly nature and decent electrochemical activity, zinc oxide can be selected as a potential material of electrode for fabrication of supercapacitor.

ZnO nanoparticles are usually synthesized by the colloidal chemical methods together with polymer stabilization, sol–gel process, reversed micelles, and also alkoxide-assisted methods [15–18]. By using these approaches, monodisperse particles of ZnO with small size (75 nm) was possible to synthesize. Nevertheless, these kinds of chemical synthesis need numerous and lengthy step by step processes which uses various organic solvents along with surfactants to make steady the nanoparticles [19]. They also propose restricted control over the dispersion and composition, resulting in agglomeration of ZnO nanoparticles with the increased quantities of defects in structure.

With controlled and limited size and high purity of chemical, physical synthesis techniques propose a facile way to the development of the ZnO nanoparticles. Physical synthesis techniques have also been broadly used to make ZnO structures with molecular beam epitaxy, chemical vapor deposition (CVD), pulsed laser deposition as well as vapor phase transport (VPT) [20–22]. The temperatures are noticed above the 500 °C, and sometimes 1000 °C in most of the physical synthesis techniques.

In this current study, an in-situ fabrication route of a thin film of ZnO nanoparticles on porous silicon substrates at temperature 900 °C reported which can be operated at atmospheric pressure. ZnO nanoparticles have been noticed to grow on porous Si (1 0 0) substrate inside a covered crucible in a horizontal tube furnace under inert condition. In this method, battery powder of spent Zn–C can easily be used as a main source of precursor which are essential for the development of ZnO nanoparticles instead of pure precursor. As far the literature survey, no study has reported on ZnO nanoparticles as an ultra-thin film manner synthesized from waste materials/waste battery and applied directly in supercapacitor application without any further modification. However, as an energy storage appliance waste carbonaceous material like bio-waste, polymers etc. have been reported, but metal oxides from waste were disregarded. Consequently, in-situ fabrication process of ZnO nanostructured thin film from spent battery for supercapacitor application will be perceptibly attractive and economically viable for large scale fabrication simultaneously diverting hazardous battery waste from landfill.

In landfill, the chemical inside the battery leaks and pollutes the land and water which causes environmental hazard and human health risk. In accordance with other countries (Directive 2006/66 of the European Commission), the Australian standard for electronic waste recycling (AS/NZS 5377:2013) does not accept the process of disposal of wasted batteries to landfill. Approximately 350 million (less than 1 kg in weight) batteries are utilized in Australia per year [23]. Primary/non-rechargeable/single-use batteries count 81% and zinc-carbon battery (Zn–C) counts 19% of the total handled batteries mostly goes to landfill [23]. Therefore, it is highly demanded to find out an appropriate and feasible solution to recover the value-added materials for various functions. Zn–C is one of the most valued sources of metal such as Zn, Mn, or oxide. Nowadays, several studies like mechanical method of separation, pyrometallurgical, hydrometallurgical and bio-hydrometallurgical treatments reported to recover value added content from wasted Zn–C batteries. However, the applications of recovered materials are not popular yet in most of the literatures studied so far.

Here, we report on the first electrochemical investigation of a bare semiconductor nanostructure-based electrodes for supercapacitance which is prepared without adding any conductive carbon materials. We choose ZnO NPs for our investigation because of its high electron mobility and synthesized these nanoparticles as an ultra-thin film manner on porous silicon substrate from spent Zn–C battery powder. Our investigations revealed that ZnO NPs based electrodes provide 547 F $g^{-1}$ specific capacitance at the 5 mV $s^{-1}$. Such performance of fabricated electrode is a promising green alternative input for high-capacitance supercapacitors for practical applications.

## 2 Experimental

### 2.1 Raw material

Cylindrical shaped spent zinc-carbon (Zn–C) battery, collected from Environmental sustainability estate management, UNSW Sydney and was used as a raw material for this investigation. Zn–C type battery is mainly made of a combination of anode (negative) and cathode (positive). Outer layer of the battery (consists of Zn) mainly works

as anode and powdered materials holding manganese dioxide ($MnO_2$) perform as cathode that is wetted along with the zinc chloride ($ZnCl_2$) solution in heavy duty Zn–C battery. The paste of $ZnCl_2$ is considered the electrolyte which can guarantee the continuous current flow. A rod of carbon has been put in centre of battery and it can act as a current conductor. Spent Zn–C battery has been dismantled to distinct zinc casing, separator, carbon rod as well as powder material holding $ZnCl_2$ as well as $MnO_2$. The obtained powder has been used for synthesis of raw material of ZnO nanostructured thin film. Before using this as raw materials, powdered materials found from spent Zn–C type battery have been dried in the oven at 60 °C for 24 h to eliminate moisture. Schematic demonstration of various components of a Zn–C type battery and also dismantled fractions of these used for this study are shown in Fig. S1.

## 2.2 In-situ fabrication method of ZnO nanostructured thin film

Figure 1 illustrates the schematic demonstration of diagram of the in-situ fabrication method of ZnO nanostructured thin film using Zn–C battery. The system is made of a furnace along with the heating zones with two variable temperatures and a source of argon (Ar) by means of the carrier gas. As demonstrated in the Fig. 1, a graphite rod has been utilized as an important support to hold ceramic crucible in the core reaction unit into heating region or area or out of furnace. A bigger view of the crucible is exhibited in the box well-defined along with a red dashed line. From the figure, it is clearly noticeable that the substrates remained away from precursor. Moreover, a controlled flow of the carrier gas has been required to reproduce the growth of the materials. At a certain temperature, the battery powder began to decompose and freed a volatile matter, which can be carried using flow of Ar gas for interaction with target substrate.

## 2.3 Substrate preparation

In synthesis process, all the used chemicals are considered analytical grade which have been purchased from Sigma-Aldrich Co. Inc. and have been used without any further purification.

For synthesise of the porous silicon (P-Si), a p-type (phosphorus-doped) (100) Si wafer (5 mm × 5 mm) which has a resistance ranging from 0.003 to 0.03 Ω cm and a thickness of 500 ± 25 mm, has been used. The wafer has been ultrasonically cleaned in methanol ($CH_3OH$), acetone ($(CH_3)_2CO$), and deionized (DI) water. After cleaning, it has been dried using nitrogen at the temperature of 100 °C for 20 min on the hot plate. Afterward, the wafer has been immersed in the solution of buffered oxide etch (BOE) for removing the layer of oxidation from Si wafer at normal temperature. Afterwards, the wafer has been immersed in solution of etchant composed of Hydrogen fluoride,

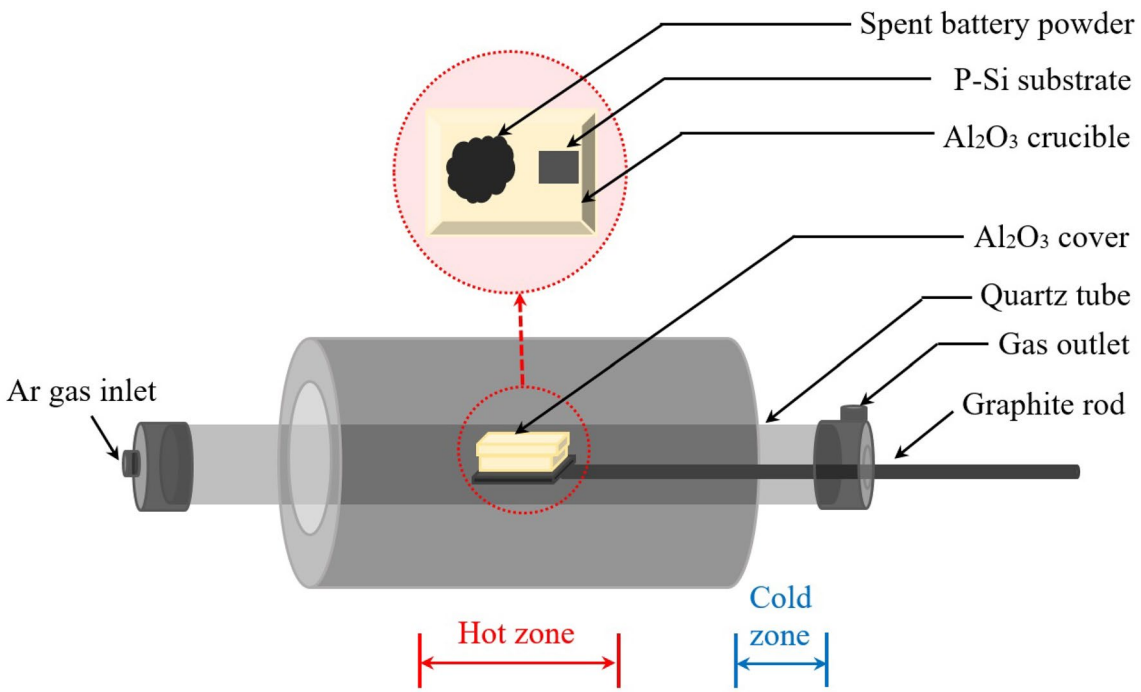


**Fig. 1** Schematics of experimental set up to fabricate ZnO NP thin film on P-Si substrate from spent Zn–C battery

Hydrogen peroxide, and DI water at a 5:2:1 volume ratio at normal temperature for 2 min in the Teflon vessel for obtaining the P-Si. Lastly, the Si wafer has been rinsed with the DI water, and dried with nitrogen at the temperature of 60 °C.

### 2.4 Characterization technique

X-ray fluorescence (XRF) of Axios Advanced WDXRF with Rh end-window tube "Supreq Software" was used for the elemental analysis of battery powder. The morphology and microstructure of this powder were observed by JEOL 7001F. Later, fabricated thin film, discussed above have extensively been characterised for examining their properties. Scanning electron microscopes (FEI Nova NanoSEM 230 and NanoSEM 450) has been used for investigation of microstructure and the surface morphology of materials.

For examining the chemical composition as well as the structure of the resultant grown nanostructures, a transmission electron microscope (Philips cm200) joined with the energy dispersive spectroscopy (EDS) and an X-Ray Photoelectron Spectroscopy (XPS) have been used. Measurements of XPS have been done by an equipped monochromatic Al anode X-ray thermo ESCALAB250Xi system and the data analysis has been carried out using Advantage software with the reference energy of 284.8 eV for adventitious C1*s*. A dual beam focused ion beam microscope (FIB, FEI Nova NanoLab 200) has been used to prepare samples for transmission electron microscopy analysis. Different phases of raw material were identified by PANalytical X'Pert Pro Multipurpose XRD using CuKα radiation. Thin film X ray diffraction (PANalytical Empyrean XRD) has been used for the study of materials structural properties. The contact angles of water droplet have been examined by contact angle goniometry (Kruss DSA 100 easy drop) using the sessile drop method along with distilled DI water droplets (about 3 µl) at normal temperature.

### 2.5 Cell fabrication and measurement

The working electrode of the supercapacitor cell was fabricated with ZnO/P-Si substrate (5 mm × 5 mm) using Cu wire as the current collector. By using the Ag paste, Cu wire was attached with the ZnO/P-Si. In addition, to avoid the more contact between sample as well as current collector of any polymer binder, for instance poly (vinylidene fluoride), or conducting agent, for example super-p was not used for preparing the device. Only, by using the Ag paste, Cu wire was attached with the ZnO/P-Si. Cyclic voltammetry (CV) and electrochemical impedance spectroscopy (EIS) have been performed at room temperature using a Biologic VSP-300 electrochemical workstation.

The supercapacitance/electrochemical studies have been done in a standard asymmetric three-electrode system consisting of in situ fabricated ZnO film as working electrode, Pt wire as a counter electrode, and saturated calomel ($Hg_2Cl_2$) electrode as a reference electrode. The electrolyte used was aqueous solution of 0.6 M KOH. CV of the unit cell was performed between − 0.5 and 0.8 V for the aqueous electrolyte at different scan rates (5–100 mV $s^{-1}$). The measurements of electrochemical impedance spectroscopy have been carried out under the open circuit voltage in an alternating current frequency range of 10 kHz–100 MHz with an excitation signal of 0.6 V.

## 3 Results and discussion

### 3.1 Characterization of spent Zn–C battery

Figure 2a illustrates the FESEM image of spent Zn–C battery powder. From the figure it was observed that, there was no orientational morphology appeared in the spent Zn–C battery powder rather than agglomerated particles. In addition, due to the co-existence of coarse and fine particles in aggregated manner, it was difficult to distinguish the sizes of the particles throughout the composition. Figure 2b shows the XRD analysis of spent battery powder where the diffraction peaks mainly showed the presence of $ZnMn_2O_4$ (hetaerolite) and $Zn_5(OH)_8Cl_2{\cdot}H_2O$ (simonkolleite) phases. EDS analysis in Fig. 2c also demonstrated the Zn, Mn, O, Cl peaks which are really high in spent battery powder. Existence of C peak is recognized as a form of carbon from in the cathode mixture and/or from carbon rod while dismantling. As discussed in the Experimental section, the powdered materials of spent Zn–C battery were characterized for the elemental analysis by XRF. According to the XRF results (shown in Fig. 2d), the powdered materials of spent Zn–C battery has 50.72% manganese (Mn), 18.67% Zinc (Zn), 7.28% chlorine (Cl), and 0.42% Iron (Fe) as major element (all compositions are expressed in weight percentage and except chlorine, other elements are in oxide form). Elemental and phase analysis of the spent Zn–C battery by EDS, XRF and XRD are compatible with each other and with existing literature of the Zn–C battery.

Figure 3 illustrates the thermogravimetric analysis (TGA) of spent battery powder at the rate of 20 °C $min^{-1}$ from normal temperature (RT) to 1200 °C under nitrogen atmosphere. From the TGA analysis, it was observed that significant weight loss of approximately 52% occurred which could be attributed to decomposition, evaporation of materials. From the figure, it is clearly visible that weight loss occurred in three major regions. First region or initial weight loss below 350 °C can be attributed to

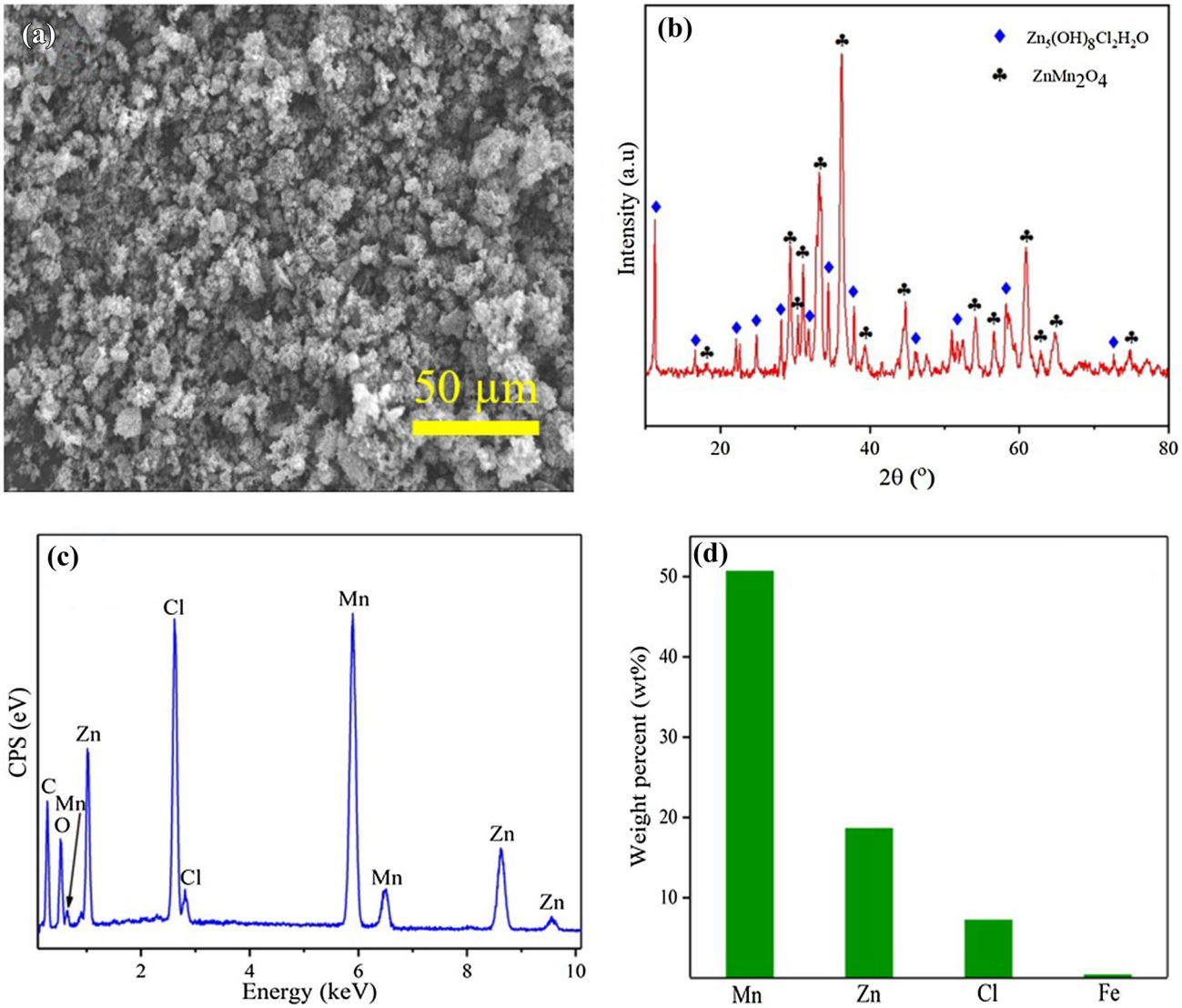


**Fig. 2** **a** FESEM image, **b** XRD pattern, **c** EDS spectra, and **d** chemical composition of spent Zn–C battery powder

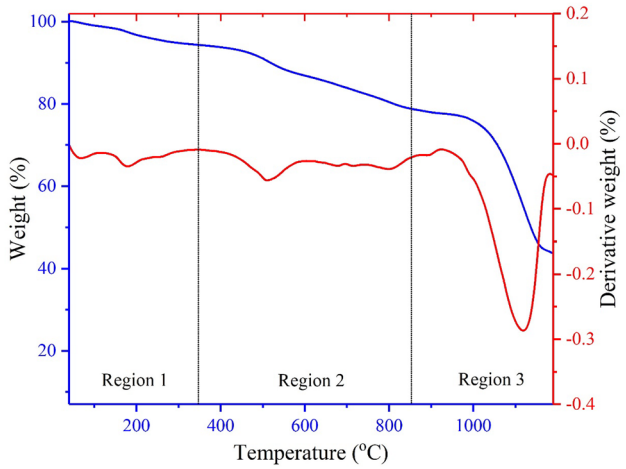


**Fig. 3** Thermogravimetric analysis of spent Zn–C battery powder

the loss of moisture. In the second region, at 450 °C to 700 °C temperature, weight loss is attributed to the oxygen/moisture loss due to decomposition of $ZnMn_2O_4$ and $Zn_5(OH)_8Cl_2{\cdot}H_2O$ phases in spent Zn–C battery [24]. Most importantly, in region three, major weight loss was observed from 800 °C, is referred to evaporation of ZnO through formation of Zn vapor. From the literature it is well known that, evaporation of Zn/ZnO mainly occurred in the temperature region in between 800 and 950 °C [24] though the TGA data showed maximum weight loss at 1150 °C due to Zn/ZnO evaporation. The optimal temperature of 900 °C is considered for this study to fabricate ZnO nanoparticles as a discrete thin film manner on P-Si substrate employing spent Zn–C battery as precursor.

### 3.2 Growth of ZnO nanoparticles as discrete ultra-thin film manner on the P-Si substrate using waste Zn–C battery as precursor

After chemical analysis, the powdered material of spent Zn–C battery was considered to the heat treatment at 900 °C to produce the needed pulp for the fabrication process of ZnO nanoparticles development on the surface of P-Si. To fabricate the ZnO nanostructured thin film, the powdered material of spent Zn–C battery samples and the porous Si substrate were kept in the covered crucible, maintaining an optimum height and were also put into the front path of the furnace (cold zone: ~ 180 °C) by the graphite rod and were placed there for 10 min. After that, the graphite rod was placed gradually to the hot area of furnace, where the high temperature was set (900 °C) and placed there for 60 min. A continuous flow of Ar gas (0.6 L $min^{-1}$) was maintained throughout the experiment. During the increasing temperature variation from cold to hot zone, simonkolleites ($Zn_5(OH)_8Cl_2.H_2O$) phase of the spent battery powder lost the single mole of water. At higher temperature (900 °C) and prolonged heating $Zn_5(OH)_8Cl_2$ decomposed to ZnO and hetareolite ($ZnMn_2O_4$) phase of the spent battery powder also started to change their phases to ZnO and MnO [25]. ZnO reduced to Zn vapor by carbothermal reduction (LECO carbon analysis showed, C ~ 9.5%) and converted to ZnO again by in-situ oxidation [26]. Due to the optimal temperature and flow of the carrier gas, formation of ZnO pulp was higher, which predominantly increased the density of the ZnO pulp inside the crucible. The lighter weight of the ZnO pulp inside the crucible chamber, facilitated the good contact with the targeted substrate. P-Si substrate can provide larger internal surface, high resistivity and strong and high surface absorbability. The wettability characteristics and surface energies of the P-Si substrate also played a vital role to form the uniform ZnO NPs ultra-thin film without agglomeration. Due to hydrophobic nature and lower surface energy of the P-Si substrate, when the pulp of ZnO came to the contact of the substrate, the grain size of ZnO became smaller along with reduced inter-grain distances and created a discrete manner ultra-thin film. The graphite rod was taken back to the cold zone after 60 min to cool down and substrate was taken out for analysis and for electrode fabrication. Figure 4 shows the overall reaction mechanism for the formation of ZnO nanoparticles as an ultra-thin film manner on P-Si substrate.

FESEM micrographs of ZnO NPs are shown in Fig. 5. The particles were semi-spherical in morphology and showed uniform distributions all over the substrate as a discrete ultra-thin film manner. Density of the nanoparticles was almost same in all over the substrate and the average diameter size of particles was ~ 45 nm. Most importantly, no aggregation and particle stacking were observed anywhere in the substrate. This could be attributed to the optimal reaction time, conditions and controlled flow of the carrier gas during the experiment [27].

The thickness of the ZnO ultra-thin film was measured by taking a cross-sectional TEM image from the ZnO/P-Si substrate and is given in Fig. 6a. The figure illustrates that ZnO ultra-thin film basically consists of several ZnO film layer which stacked with each other periodically and made one thin layer. It was observed that uniform pores formed in between every two layers which made the ultra-thin film as discrete. The thickness of the ultra-thin film was around ~ 390 nm, where the single layer was ~ 45 nm. The amount

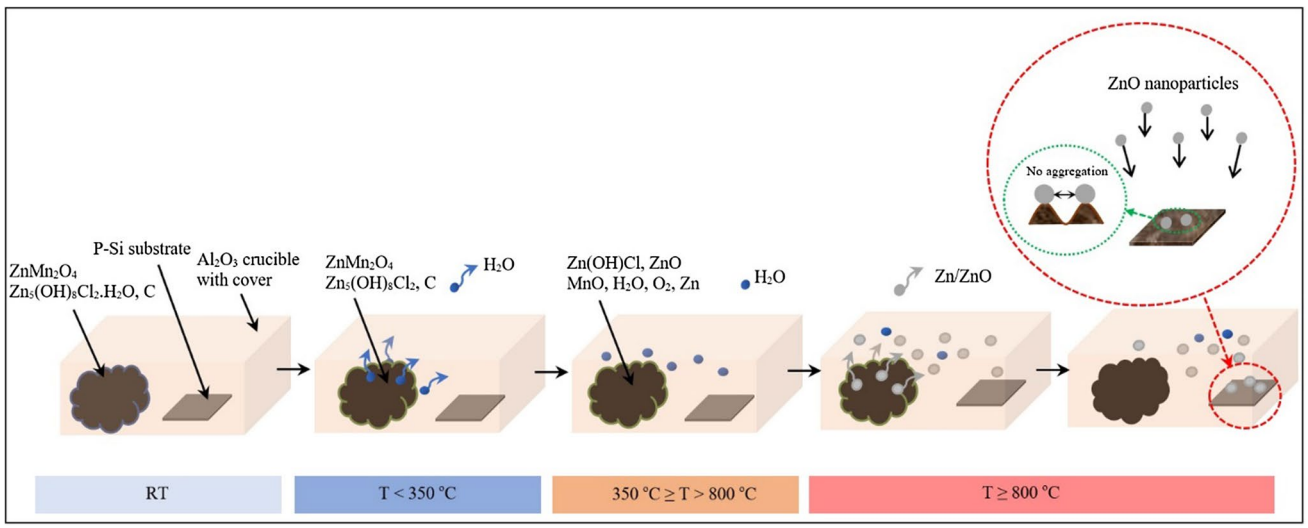


**Fig. 4** Schematics of steps of in-situ fabrication of ZnO NP thin film on P-Si substrate from spent Zn–C battery

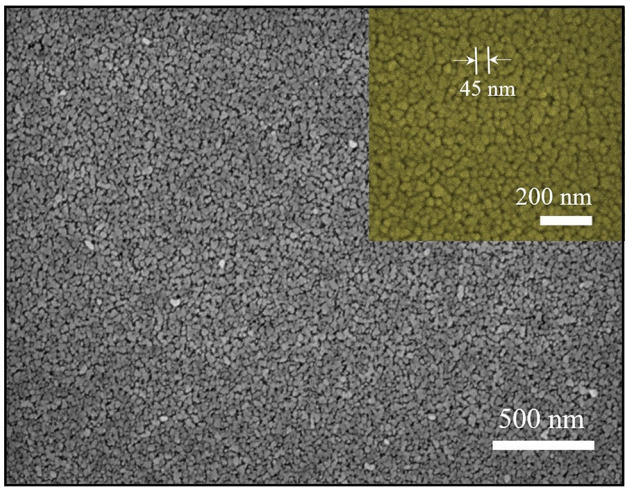


**Fig. 5** FESEM images of synthesized ZnO nanoparticles on P-Si substrate as discrete ultra-thin manner (inset shows the average diameter of ZnO NPs)

of layers in ultra-thin film could be controlled by changing the time of deposition. To confirm the distribution of ZnO on the surface of lattice, elemental mapping has been done and the results have been depicted in the Fig. 6b–d. The analysis refers that Zn and O which are spread homogenously over the entire P-Si substrate, and it further confirms the formation of extremely uniform ZnO film.

The elemental composition of as-synthesized ZnO film on the P-Si substrate was characterized by EDS spectra (Fig. 7a). The existence of several peaks of zinc (Zn), oxygen (O), and Silicon (Si) and the lack of any peaks associated with contaminants, settled the formation of a pure nanostructured material which was further confirmed by XRD analysis. The relatively low counts of nanomaterial (Zn, O) proposed the formation of the ultra-thin film over the porous Si substrate. In addition, EDS mapping analysis confirms the homogeneous property of the nanoparticles all over the substrate (Fig. S2). Figure 7b illustrates the X-ray diffraction (XRD) patterns of the synthesized pure ZnO NPs on the porous Si substrates. The presence of peaks

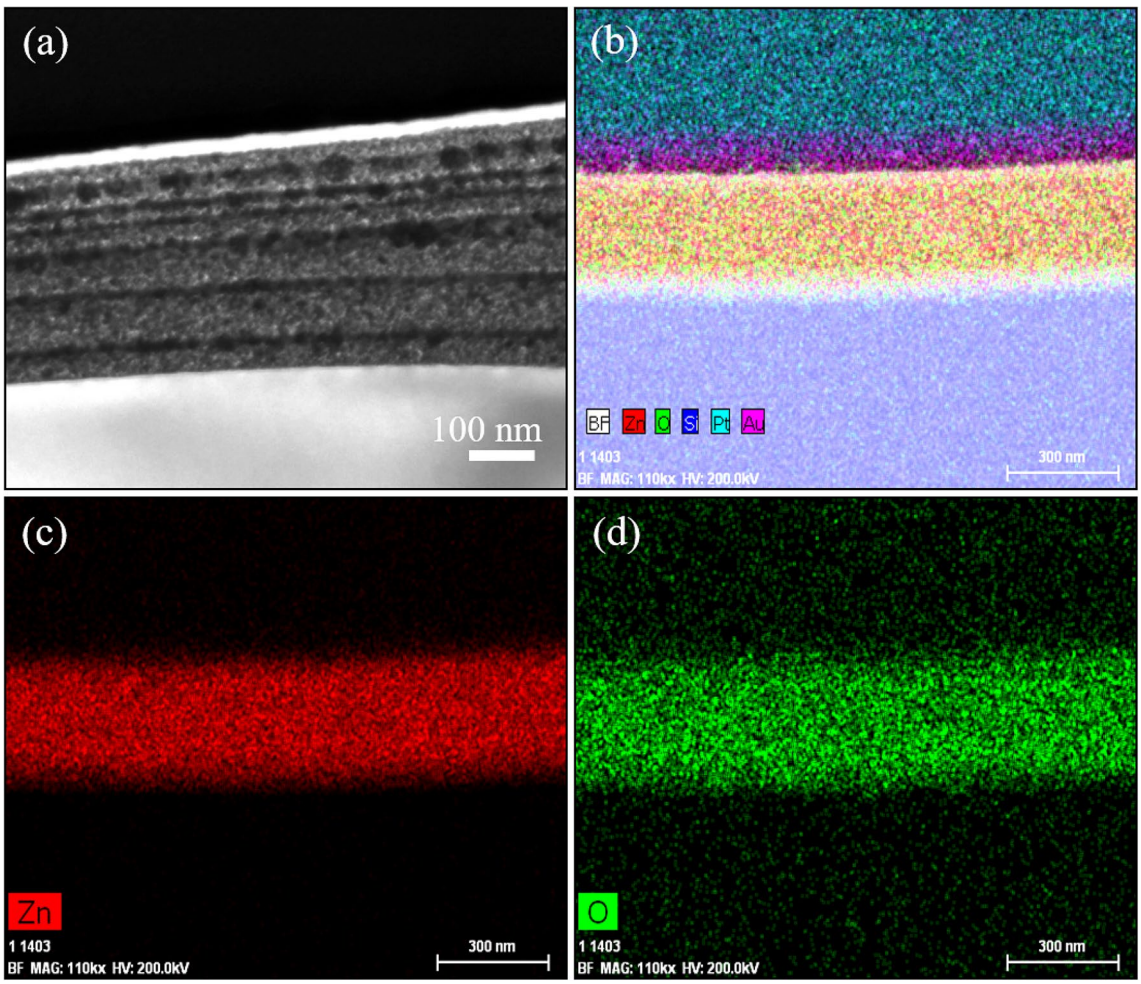


**Fig. 6** **a** Cross-sectional dark field TEM image and **b**–**d** elemental mapping of ZnO ultra-thin film on P-Si substrate

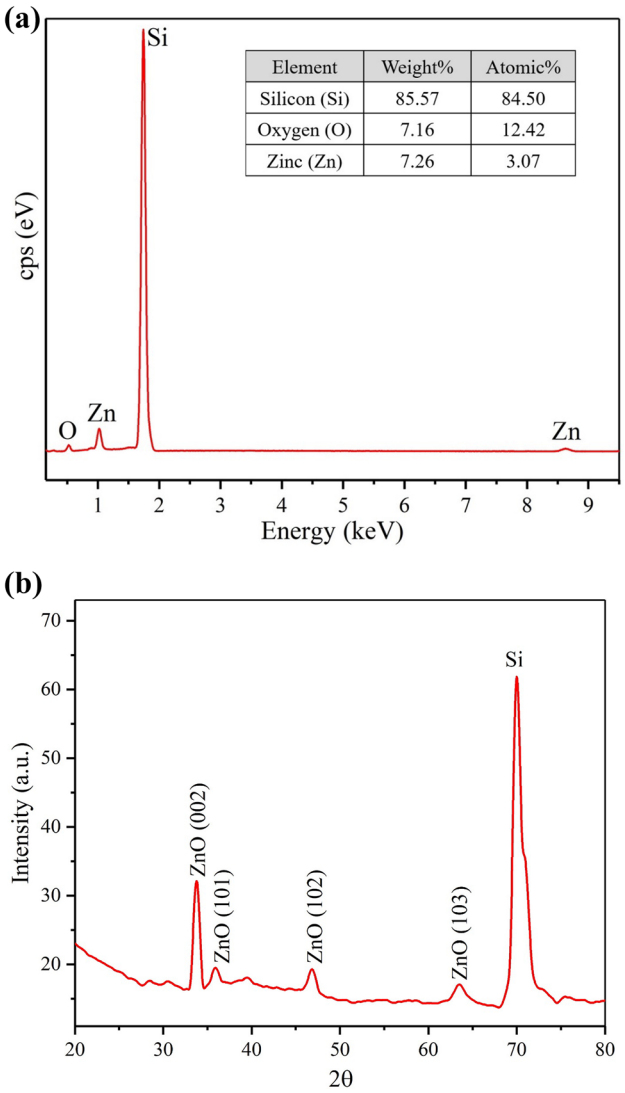


| Element | Weight% | Atomic% |
|---|---|---|
| Silicon (Si) | 85.57 | 84.50 |
| Oxygen (O) | 7.16 | 12.42 |
| Zinc (Zn) | 7.26 | 3.07 |

**Fig. 7** **a** Typical EDS spectrum and **b** XRD pattern of ZnO NPs/P-Si

of characteristic diffraction for pure ZnO corresponding to (002), (101), (102), and (103) planes at $2\theta = 33.8°$, 35.9°, 46.8°, and 63.5°, respectively, are in good agreement with standard XRD peaks of crystalline ZnO with a hexagonal wurtzite structure (JCPDS card No. 36-1451) [28, 29]. There is not found any characteristic peaks from the intermediates for instance $Zn(OH)_2$ in the samples. This result refers the formation of high purity of the ZnO NPs. The estimated crystalline size of the ZnO nanoparticles have been measured from the dominant peak (002) using formula of Scherrer and has been found to be about 47 nm.

To calculate the surface energy and wettability of ZnO NPs deposited on porous Si substrate, characterization of the water droplets is carried out. The Young's equation refers the equilibrium forces among the tensions of surface at a 3 phase boundary. The equation is as follows,

$$\cos\theta_w = \gamma_{sv} - \frac{\gamma_{sl}}{\gamma_{lv}} \quad (1)$$

where $\gamma_{sv}$, $\gamma_{lv}$ and $\gamma_{sl}$, and refers the energies of surface of the solid–vapor, liquid–vapor interfaces and solid–liquid, correspondingly, and $\theta_w$ refers the equilibrium contact angle. Contact angle images of bare porous Si substrate, and of ZnO NPs on P-Si are shown in Fig. 8. From the literature, it is familiar that if $\theta_w > 90°$, the surface will be hydrophobic, and otherwise the surface will be hydrophilic; thus, the modified porous Si substrate was highly hydrophobic in nature [30]. On the other hand, the deposition of ZnO NPs on the P-Si substrates made the modified substrate more hydrophilic.

This hydrophilic property of the ZnO NPs/P-Si can be suitable for the application as electrode in aqueous electrolyte based electrochemical capacitors. Since this kind of property can offer a highly wettable, superabsorbent and ionized material in electrochemical solution, it can increase accessibility of the pores and can facilitate ion transport within the electrode [31]. Furthermore, surface roughness remains directly proportional to the contact angle and therefore inversely proportional to the energy of surface [30]. It can be considered that surface roughness and chemical composition are the key factors to determine the surface energy of the thin films. To calculate the

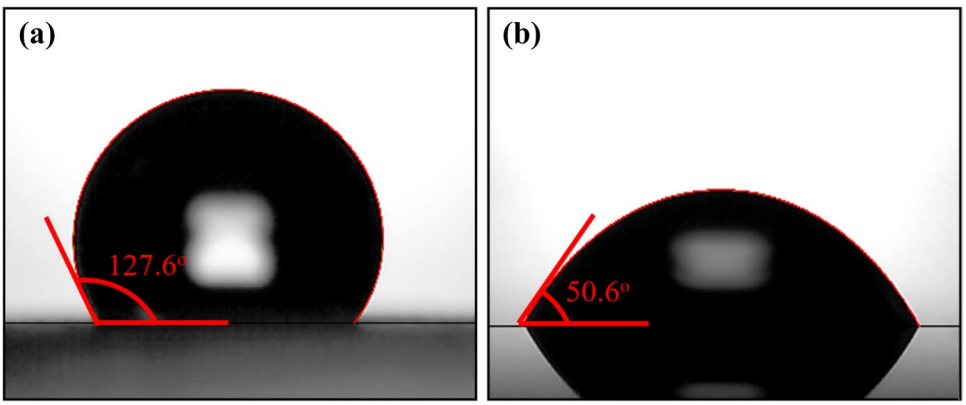


**Fig. 8** Contact angle images of **a** porous Si, and **b** ZnO NPs/P-Si

surface energy, the equation of Owens and Wendt and that of Wu were each used; these are presented as Eqs. (2) and (3), respectively.

$$\gamma_{sl} = \gamma_{sv} + \gamma_{lv} - 2\left(\sqrt{\gamma_{sv}^{D}\gamma_{lv}^{D}} + \sqrt{\gamma_{sv}^{p}\gamma_{lv}^{p}}\right) \quad (2)$$

$$\gamma_{sl} = \gamma_{sv} + \gamma_{lv} - 4\left(\frac{\gamma_{lv}^{D} \times \gamma_{sv}^{D}}{\gamma_{lv}^{D} + \gamma_{sv}^{D}} + \frac{\gamma_{lv}^{P} \times \gamma_{sv}^{P}}{\gamma_{lv}^{P} + \gamma_{sv}^{P}}\right) \quad (3)$$

Here, $\gamma_{lv}^{D}$, $\gamma_{sv}^{D}$ and $\gamma_{lv}^{p}$, $\gamma_{sv}^{p}$ refer the dispersive and also polar components of liquid–vapor ($\gamma_{lv}$) energy and solid–vapor ($\gamma_{sv}$) energy, correspondingly. The energy of surface has been measured for entire samples in the same way. The lower contact angle of the ZnO NPs/P-Si specifies the maximum surface energy. Table 1 shows the measured surface energies and contact angles for both samples.

ZnO NPs/P-Si was analysed by the X-ray photoelectron spectroscopy (XPS). Figure 9a demonstrates the usual XPS with widespread survey spectra of the ZnO nanoparticles. From the figure it was observed that Zn, O, and C peaks have been spotted in survey spectra with minor impurity. The spotted carbon is associated with the adsorbed carbon on the surface at time of exposure of the sample to the ambient atmosphere. Total binding energies have been corrected for the charge shift by the C1*s* peak of graphitic carbon (BE = 284.6 eV) as a Ref. [32]. From Fig. 9b and Table 2, it was observed that the Zn 2*p* core-level of ZnO NPs has two fitting peaks located at about 1044.6 and 1021.5 eV attributed to Zn $2p_{1/2}$ and Zn $2p_{3/2}$, respectively [33]. These results refer that the chemical valence of Zn at the surface of the nanoparticles is in oxidation state. For the ZnO nanoparticles, the binding energy difference between the Zn $2p_{1/2}$ and Zn $2p_{3/2}$ was 23.1 eV. Figure 9c displays XPS spectra of O1*s* region of ZnO nanoparticles. The O1*s* core-level spectrum of ZnO nanoparticles showed three

**Table 1** Contact angles and calculated surface energy of porous silicon, and ZnO NPs/P-Si

| Sample | Contact angle (°) | Owens–Wendt method | | | Wu method | | |
|---|---|---|---|---|---|---|---|
| | | $\gamma_{sv}$ (mN/m) | $\gamma_{sv}^{D}$ (mN/m) | $\gamma_{sv}^{p}$ (mN/m) | $\gamma_{sv}$ (mN/m) | $\gamma_{sv}^{D}$ (mN/m) | $\gamma_{sv}^{p}$ (mN/m) |
| Porous Si (P-Si) | 127.6 | 0.0075 | 0.0075 | 0.0075 | −5 | −1.259 | −2.7 |
| ZnO NPs/P-Si | 50.6 | 70.85 | 31.69 | 39.46 | 79.02 | 41.32 | 37.69 |

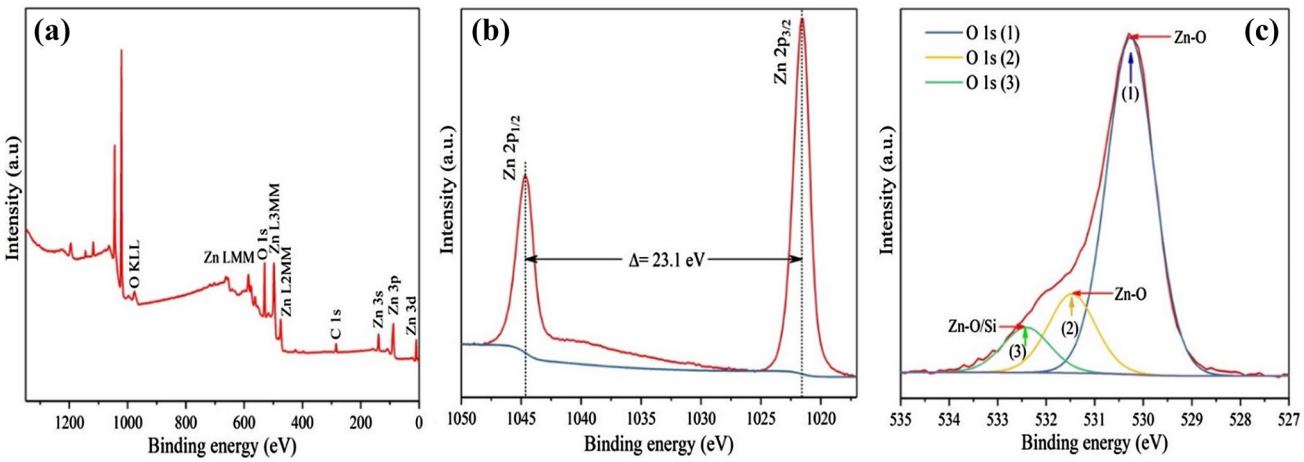


**Fig. 9** XPS spectra of **a** survey spectra, **b** Zn 2*p*, and **c** O1*s* for ZnO NPs/P-Si

**Table 2** XPS analysis of ZnO nanoparticles

| Peak | Position BE (eV) | FWHM (eV) | Raw area (cps eV) | Atomic Conc. (%) |
|---|---|---|---|---|
| Zn 2*p* | 1021.57 | 1.57 | 830,124.83 | 40.74 |
| O1*s* (1) | 530.26 | 1.15 | 64,849.36 | 27.49 |
| O1*s* (2) | 531.47 | 1.15 | 15,239.58 | 6.46 |
| O1*s* (3) | 532.41 | 1.15 | 8694.1 | 3.69 |

different forms of oxygen. Three fitting Gaussians peaks marked as (1), (2) and (3) were used to fit the experimental data. Peak (1) and (2), positioned at the lower binding energy of 530.26 eV and 531.47 eV is assigned to $O^{2-}$ ions in the Zn–O bonding of the wurtzite structure of ZnO [33]. The other peak (3) located at 532.41 eV is related to Zn–O/Si. Binding energy (BE) in eV for the core levels Zn 2*p* and O1*s* and their related full-width at half maximum (FWHM) with the respective atomic concentrations are listed in Table 2. The results demonstrate that the O/Zn ratio is a little lower than unity which confirms that the synthesized nanostructures are pure ZnO as confirmed by XRD and EDS results.

### 3.3 Electrochemical analysis

The overall performance of ZnO NP based electrode has been analysed using electrochemical impedance spectroscopy (EIS) as well as cyclic voltammetry (CV). Figure 10a

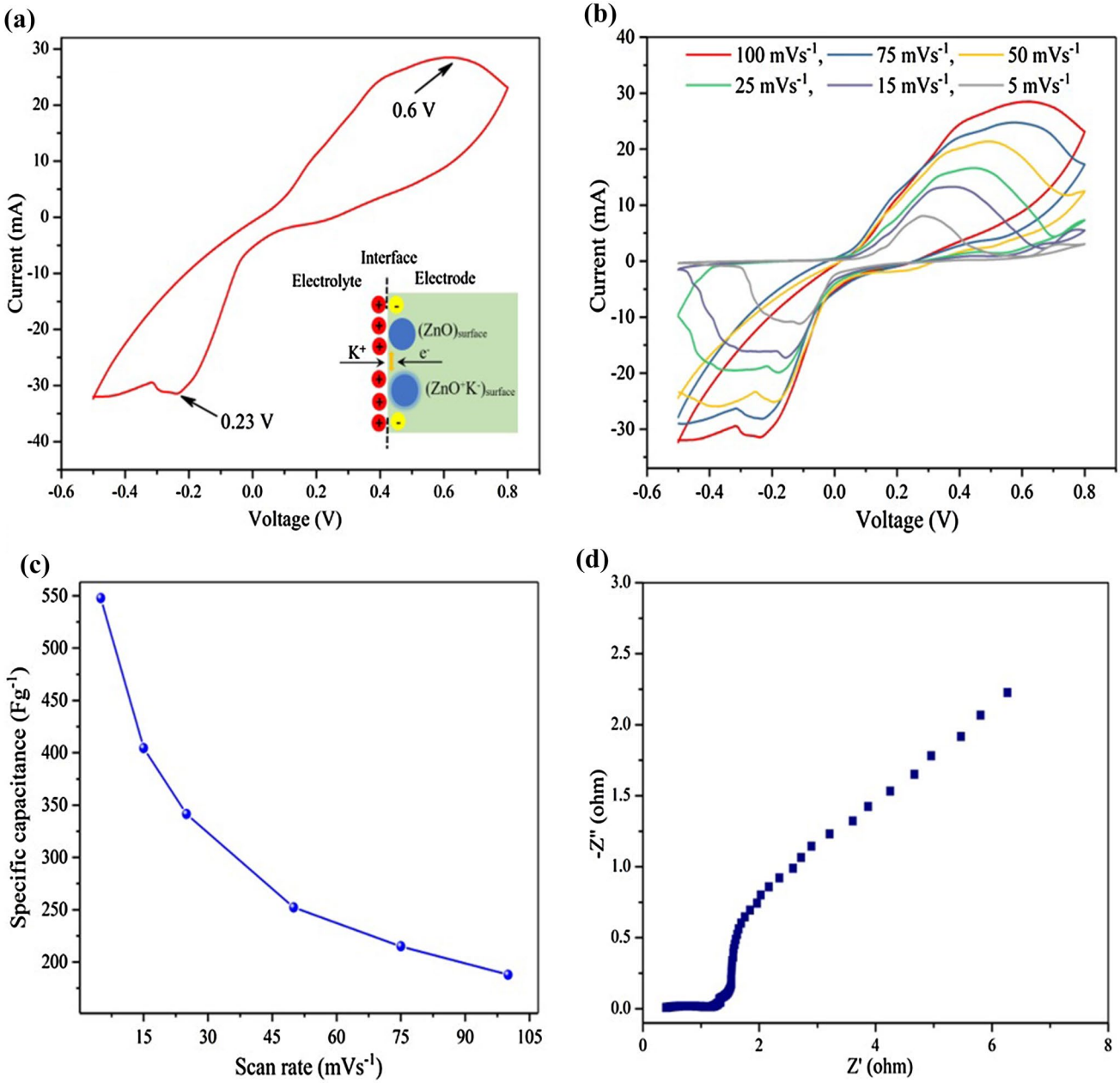


**Fig. 10** Electrochemical performance of the ZnO NPs/P-Si in 0.6 M KOH (aq.) electrolyte at room temperature: **a** CV at a scan rate of 100 mV $s^{-1}$ (inset shows the charge transfer across interface through surface redox reaction), **b** CV curves at different scan rates (from 100 to 5 mV $s^{-1}$), **c** specific capacitance as a function of a different scan rates, and **d** Nyquist plots of the ZnO NPs/P-Si electrode

illustrates the CV curve over a voltage range from − 0.5 to 0.8 V for the ZnO/P-Si based electrodes measurement at a scan rate of 100 mV $s^{-1}$ in 0.6 M KOH electrolyte. From the figure, two peaks at − 0.23 V and 0.6 V can obviously be observed, caused by redox reaction between the ZnO and electrolyte. The redox process is primarily governed by intercalation as well as deintercalation of $K^+$ from electrolyte into ZnO: $ZnO + K^+ + e^- \leftrightarrow ZnOK$ [34, 35]. These outcomes proposed that the high specific capacitance related to ZnO electrode that originated from pseudocapacitance of the electrochemically active ZnO NPs. Figure 10b demonstrates the CV curves for the as-fabricated electrode at a scan rate of 5 mV $s^{-1}$ to 100 mV $s^{-1}$. As an essential parameter, the specific capacitance ($C_{sp}$) has extensively been used to calculate the overall performance of the electrochemical supercapacitors, and it can be measured by dividing the capacitance by total weight of the deposited ZnO, that is:

$$C_{sp} = \frac{1}{w\Delta V}\int_{y}^{x} idt \quad (4)$$

where i refers the current density, t refers the time, x and y refers the time at lowest and highest voltage range (V), ΔV refers the potential window width (in V) and w refers the sample weight.

It appears to be familiar that a higher $C_{sp}$ value than a wide range of scan rates is actually significant for a material for real time application in supercapacitors. Figure 10c demonstrates the differences in specific capacitance of ZnO NPs as a function of scan rates. From the figure it is clearly visible that, with the rise of scan rate from 5 to 100 mV $s^{-1}$ the specific capacitance decreased. At the high scan rates, the movement of the electrolyte ions are bounded by diffusion because of the time restrictions, and simply the outer active surface is employed for storage of charge, thus at high scan rate specific capacitance value was low. At lower scan rates, all the active surface areas of ZnO thin film can be used for storage of charge and the highest specific capacitance of 547 F $g^{-1}$ was achieved at 5 mV $s^{-1}$ scan rate for the ZnO/P-Si electrode. The discrete structure of ZnO NPs not only inhibited the stacking of the porous silicon substrate as film manner, similarly improved the electrochemical uses of ZnO NPs. Along with this, the outstanding interfacial contact and enlarged contact area among several layers of ZnO thin film (Fig. 6a) could potentially increase the nanoparticles accessibility to the electrolyte ions and could also shorten the ion diffusion plus migration pathways.

The EIS is one kind of analysis which is fundamental technique to examine significant behaviour of the electrode materials for the supercapacitors. The EIS data has been examined by Nyquist plots. These plots which demonstrate the response of frequency of the electrode/electrolyte system, are plotted with − Z″ (imaginary component) of impedance against the Z′ (real component) (Fig. 10d). The impedance of ZnO/P-Si electrodes have been measured over the frequency ranges of 0.1 Hz–100 kHz. However, the impedance plots have been drawn of a straight line in low frequency range and also a semicircle arc in high frequency range. The high frequency arc relates to the transfer of charge limiting process which is also ascribed to capacitance ($C_p$) in parallel through charge transfer resistance ($R_{ct}$) at the interaction interface between the electrode and solution of electrolyte. $R_{ct}$ can directly be measured as a semicircle diameter. The charge-transfer resistance ($R_{ct}$) are caused by the Faradaic reactions on the grain surface. It is identified that the as-fabricated electrode has a low $R_{ct}$ (6.5 Ω) value as a result

**Table 3** Summary of reported electrochemical performance for metal oxides and metal oxide composites

| Materials | Synthesis method | Electrolytes | Scan rate (mV $s^{-1}$) | Operating temperature (°C) | Specific capacitance (F $g^{-1}$) | References |
|---|---|---|---|---|---|---|
| AC-RuOx composite | Chemical route followed by sol–gel method | 0.1 M $H_2SO_4$ | 1 | 25 | 1580 | [3] |
| $MnO_2$/Ni foil | (a) Sol–gel method<br>(b) Electrochemical deposition | 0.1 M $Na_2SO_4$ | 50 | 25 | (a) 566<br>(b) 311 | [9] |
| (a) Pure ZnO<br>(b) Bare rGO<br>(c) ZnO/rGO Composities | (a) Chemical route<br>(b) Hummer method<br>(c) Chemical route | 0.1 M $Na_2SO_4$ | 5 | 25 | (a) 135<br>(b) 157<br>(c) 308 | [33] |
| $CoO_x$ xerogel | Sol–gel method | 1 M KOH | 5 | 150 | 291 | [8] |
| NiO/Au | Electrochemical deposition | 3 M KOH | 5 | 300 | 104 | [7] |
| NiO/Ni composite | Electrochemical deposition | 1 M KOH | – | 25 | 64 | [6] |
| Mesoporous $RuO_2$ | Chemical route | 2.5 M $H_2SO_4$ | 50 | 25 | 58 | [2] |
| ITO-Graphene-ZnO | USP followed by hummer method | 1 M KCl | 100 | 25 | 11.3 | [32] |
| ZnO/P-Si | In-Situ fabrication from spent Zn–C battery | 0.6 M KOH | 5 | 25 | 547 | This study |

of the incorporation of the ZnO, which improves the performance of charge transfer in the fabricated electrodes. In the low frequency ranges, there notice a straight line associated with the diffusive resistance or Warburg resistance of electrolyte into the electrode interior and ion diffusion/transport into the surface of electrode. The nearly vertical shape which represents the swift of ion diffusion in the electrolyte and also adsorption in the surface of electrode, also suggestes an perfect capacitive behaviour of electrodes.

A comparative table of other metal oxide and metal oxide composites with their maximum values of specific capacitance, synthesis methods, operating temperature from literature are summarised in Table 3. It has been found that the thin film of fabricated ZnO electrode using spent Zn–C battery showed promising capacitance value compared to other oxides except RuO. Future investigations will be carried out to improve the capacitance value by changing the ZnO morphology and/or making composite electrodes.

## 4 Conclusions

This study opens new opportunity of ZnO NPs electrodes fabrication using spent Zn–C battery powder as precursor for supercapacitor application. As confirmed by analysis of SEM and also TEM, the fabricated ZnO NPs were placed on P-Si substrate as the manner of ultra-thin film and contained nanopores in between stacking film layer. XRD and EDS analysis confirm the purity of the synthesized active materials. The electrochemical studies of electrode based on this ZnO NPs showed the highest specific capacitance of about 547 F $g^{-1}$ in 0.6 M KOH electrolyte at 5 mV $s^{-1}$ scan rates. This study expands opportunities to revive waste battery as an effective material for fabricating electrodes for energy storage applications.

**Acknowledgement** We gratefully acknowledge the technical support provided by Dr. Charlie Kong from Analytical Centre in the UNSW Australia for the focused ion beam (FIB) workstation.

### Compliance with ethical standards

**Conflict of interest** The authors declare no competing financial interest.

## References

1. Winter M, Brodd RJ (2004) What are batteries, fuel cells, and supercapacitors?. ACS Publications, Washington
2. Subramanian V, Hall SC, Smith PH, Rambabu B (2004) Mesoporous anhydrous $RuO_2$ as a supercapacitor electrode material. Solid State Ionics 175(1–4):511–515
3. Mahmoud AED, Stolle A, Stelter M (2018) Sustainable synthesis of high-surface-area graphite oxide via dry ball milling. ACS Sustain Chem Eng 6(5):6358–6369
4. Hu C-C, Chen W-C (2004) Effects of substrates on the capacitive performance of $RuO_x{\cdot}nH_2O$ and activated carbon–$RuO_x$ electrodes for supercapacitors. Electrochim Acta 49(21):3469–3477
5. Liu Y, Zhou F, Ozolins V (2011) Ab initio study of the charge-storage mechanisms in $RuO_2$-based electrochemical ultracapacitors. J Phys Chem C 116(1):1450–1457
6. Liu KC, Anderson MA (1996) Porous nickel oxide/nickel films for electrochemical capacitors. J Electrochem Soc 143(1):124–130
7. Srinivasan V, Weidner JW (1997) An electrochemical route for making porous nickel oxide electrochemical capacitors. J Electrochem Soc 144(8):L210–L213
8. Srinivasan V, Weidner JW (2000) Studies on the capacitance of nickel oxide films: effect of heating temperature and electrolyte concentration. J Electrochem Soc 147(3):880–885
9. Lin C, Ritter JA, Popov BN (1998) Characterization of sol–gel-derived cobalt oxide xerogels as electrochemical capacitors. J Electrochem Soc 145(12):4097–4103
10. Pang SC, Anderson MA, Chapman TW (2000) Novel electrode materials for thin-film ultracapacitors: comparison of electrochemical properties of sol–gel-derived and electrodeposited manganese dioxide. J Electrochem Soc 147(2):444–450
11. Chae DW, Kim BC (2006) Effects of zinc oxide nanoparticles on the physical properties of polyacrylonitrile. J Appl Polym Sci 99(4):1854–1858
12. Nomura K, Ohta H, Ueda K, Kamiya T, Hirano M, Hosono H (2003) Thin-film transistor fabricated in single-crystalline transparent oxide semiconductor. Science 300(5623):1269–1272
13. Yoshida T, Komatsu D, Shimokawa N, Minoura H (2004) Mechanism of cathodic electrodeposition of zinc oxide thin films from aqueous zinc nitrate baths. Thin Solid Films 451:166–169
14. Liu Y, Liu Y, Liu Y, Shen D, Lu Y, Zhang J, Fan X (2002) Structural and optical properties of nanocrystalline ZnO films grown by cathodic electrodeposition on Si substrates. Physica B 322(1–2):31–36
15. Perea DE, Hemesath ER, Schwalbach EJ, Lensch-Falk JL, Voorhees PW, Lauhon LJ (2009) Direct measurement of dopant distribution in an individual vapour–liquid–solid nanowire. Nat Nanotechnol 4(5):315
16. Comini E (2006) Metal oxide nano-crystals for gas sensing. Anal Chim Acta 568(1–2):28–40
17. Pauzauskie PJ, Yang P (2006) Nanowire photonics. Mater Today 9(10):36–45
18. Patete JM, Peng X, Koenigsmann C, Xu Y, Karn B, Wong SS (2011) Viable methodologies for the synthesis of high-quality nanostructures. Green Chem 13(3):482–519
19. Pan ZW, Dai ZR, Ma C, Wang ZL (2002) Molten gallium as a catalyst for the large-scale growth of highly aligned silica nanowires. J Am Chem Soc 124(8):1817–1822
20. Joshi RK, Hu Q, Alvi F, Joshi N, Kumar A (2009) Au decorated zinc oxide nanowires for CO sensing. J Phys Chem C 113(36):16199–16202
21. Huang MH, Wu Y, Feick H, Tran N, Weber E, Yang P (2001) Catalytic growth of zinc oxide nanowires by vapor transport. Adv Mater 13(2):113–116
22. Wang X, Summers CJ, Wang ZL (2004) Large-scale hexagonal-patterned growth of aligned ZnO nanorods for nano-optoelectronics and nanosensor arrays. Nano Lett 4(3):423–426
23. Australian Battery Recycling Initiative (ABRI) (2010) Analysis of battery consumption, recycling and disposal in Australia. Warnken Industrial and Social Ecology Pty Ltd
24. Farzana R, Rajarao R, Hassan K, Behera PR, Sahajwalla V (2018) Thermal nanosizing: novel route to synthesize manganese oxide

and zinc oxide nanoparticles simultaneously from spent Zn–C battery. J Clean Prod 196:478–488
25. Song MS, Nahm S, Cho WI, Lee C (2015) Enhanced electrochemical performance of a ZnO–MnO composite as an anode material for lithium ion batteries. Phys Chem Chem Phys 17(36):23496–23502
26. Rasines I, de Setién JM (1980) Thermal analysis of β-$Co_2(OH)_3Cl$ and $Zn_5(OH)_5Cl_2{\cdot}H_2O$. Thermochim Acta 37(2):239–246
27. Hassan K, Uddin AI, Chung G-S (2016) Fast-response hydrogen sensors based on discrete Pt/Pd bimetallic ultra-thin films. Sens Actuators B Chem 234:435–445
28. Bai S, Guo T, Li D, Luo R, Chen A, Liu CC (2013) Intrinsic sensing properties of the flower-like ZnO nanostructures. Sens Actuators B Chem 182:747–754
29. Guo W, Liu T, Zhang H, Sun R, Chen Y, Zeng W, Wang Z (2012) Gas-sensing performance enhancement in ZnO nanostructures by hierarchical morphology. Sens Actuators B Chem 166:492–499
30. Hassan K, Uddin AI, Chung G-S (2016) Hydrogen sensing properties of Pt/Pd bimetal decorated on highly hydrophobic Si nanowires. Int J Hydrogen Energy 41(25):10991–11001
31. Lee K-T, Tsai C-B, Ho W-H, Wu N-L (2010) Superabsorbent polymer binder for achieving $MnO_2$ supercapacitors of greatly enhanced capacitance density. Electrochem Commun 12(7):886–889
32. Wagner C, Gale L, Raymond R (1979) Two-dimensional chemical state plots: a standardized data set for use in identifying chemical states by X-ray photoelectron spectroscopy. Anal Chem 51(4):466–482
33. Das J, Pradhan S, Sahu D, Mishra D, Sarangi S, Nayak B, Verma S, Roul B (2010) Micro-Raman and XPS studies of pure ZnO ceramics. Physica B 405(10):2492–2497
34. Zhang Y, Li H, Pan L, Lu T, Sun Z (2009) Capacitive behavior of graphene–ZnO composite film for supercapacitors. J Electroanal Chem 634(1):68–71
35. Chen Y-L, Hu Z-A, Chang Y-Q, Wang H-W, Zhang Z-Y, Yang Y-Y, Wu H-Y (2011) Zinc oxide/reduced graphene oxide composites and electrochemical capacitance enhanced by homogeneous incorporation of reduced graphene oxide sheets in zinc oxide matrix. J Phys Chem C 115(5):2563–2571